

# Topological hybridisation of plasmons with ferrimagnetic magnons

Cooper Finnigan,<sup>1,\*</sup> Mehdi Kagarian,<sup>2</sup> and Dmitry K. Efimkin<sup>1,†</sup>

<sup>1</sup>*School of Physics and Astronomy, Monash University, Victoria 3800, Australia*

<sup>2</sup>*Department of Physics, Sharif University of Technology, Tehran 14588-89694, Iran*

(Dated: January 28, 2026)

We study the formation of hybrid plasmon-magnon modes in a heterostructure comprising a monolayer semiconductor with strong Rashba spin-orbit coupling — specifically, Janus transition-metal dichalcogenides (TMDs) — and an insulating ferrimagnet, such as yttrium iron garnet-based compounds. Using a combined microscopic-macroscopic framework for plasmon-magnon coupling, we show that plasmons and magnons strongly hybridize over both GHz and THz frequency ranges, enabling experimental access well above cryogenic temperatures. Moreover, the developed approach provides an efficient and natural classification of the topology of the hybrid modes, rooted in the phase winding of the plasmon-magnon coupling induced by spin-momentum locking and the associated chiral winding of the electronic spin along the Fermi contours. Finally, we identify experimentally accessible manifestations of the hybridization, such as topological interface modes and an anomalous thermal Hall response.

## I. INTRODUCTION

Over the last decade, magnetic heterostructures have attracted intense and growing interest as a platform for both fundamental studies and spintronic applications [1–3]. By interfacing magnetic order with electronic or collective degrees of freedom, these systems host a remarkably broad range of phenomena, including spin transport and spin-transfer torques [4], spin Hall magnetoresistance [5], and anomalous Hall effects up to their quantized limit [6]. More recently, magnetic heterostructures have also been explored as a setting for emergent collective behavior, such as magnon-mediated superconductivity [7–11] and superconducting spintronics [12, 13].

Recently, magnetic heterostructures have emerged as a promising platform for engineering strong coupling between magnons and plasmons [14–18] or surface plasmon-polaritons [19–22], and the resulting hybrid modes can be classified as topologically nontrivial [14]. This development is motivated more broadly by the growing recognition of, and interest in, beyond-electron topological physics, which can also emerge in systems where collective modes of distinct physical origin hybridize. Prominent examples include exciton-polaritons [23], magnon-phonon hybrid modes [24–26], Weyl helicon-phonon modes [27], and engineered phonon-polariton modes in photonic metasurfaces [28], where mode mixing gives rise to robust trapped modes and anomalous transport phenomena.

To date, however, experimental realizations of topological plasmon-magnon modes have not yet been reported. One major obstacle is the mismatch of characteristic energy scales: ferromagnetic magnons typically reside in the GHz frequency range, such that achieving strong coupling to plasmons requires cryogenic (often sub-kelvin)

temperatures and exceptionally high plasmonic quality factors. While such conditions can be realized in noble metals and graphene, they are considerably more challenging to achieve on the surfaces of topological insulators and in monolayer semiconductors with strong spin-orbit coupling, where plasmon-magnon interactions have been argued to be enhanced [14, 15]. It is therefore highly desirable to extend strong plasmon-magnon coupling — and the associated topological phenomena — into the THz frequency range. In this regime, plasmons in two-dimensional materials have been extensively studied, and the requirements for reaching the strong-coupling limit are substantially more favorable [29–32].

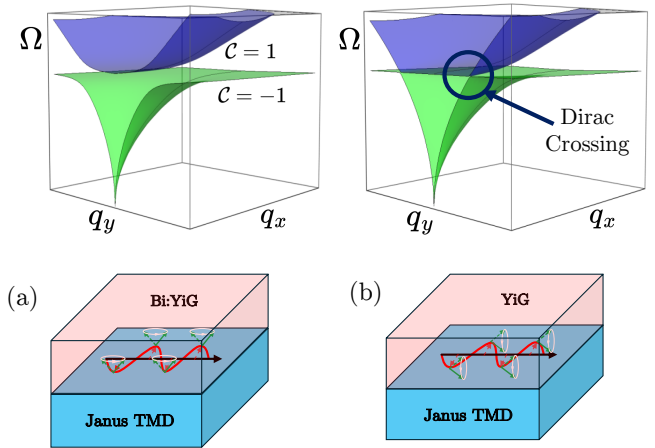


FIG. 1. Illustration of a Janus TMD interfaced with an insulating ferrimagnet for (a) *out-of-plane* and (b) *in-plane* magnetization, together with sketches of the corresponding hybrid plasmon-magnon spectra. Black (red) arrows denote electron current (spin) oscillations, while precessing green arrows indicate magnetization fluctuations. For out-of-plane magnetization, the spectrum is gapped and isotropic, exhibiting nonzero topological Chern numbers. For in-plane magnetization, the spectrum exhibits a pair of Dirac branch-crossing nodes and is strongly anisotropic.

\* [cooper.finnigan@monash.edu](mailto:cooper.finnigan@monash.edu)

† [dmitry.efimkin@monash.edu](mailto:dmitry.efimkin@monash.edu)

In this paper, we investigate the magnetic proximity effect between a Rashba electron gas in a monolayer semiconductor with broken inversion symmetry — such as a Janus transition-metal dichalcogenides (e.g., MoSeTe or WSeTe) [33–35] — and an insulating ferrimagnet, such as yttrium iron garnet (YIG) [36, 37] or its Bi-substituted counterpart (Bi:YIG) [38]. Owing to spin-momentum locking of Rashba electrons, plasmon excitations exhibit coupled charge- and spin-density oscillations and therefore interact efficiently with magnetic fluctuations across the interface. We show that both magnon branches, carrying opposite helicities, hybridize with plasmons, giving rise to mixed plasmon-magnon modes spanning frequency ranges from the GHz to the THz regime. This behavior reflects the presence of a finite magnetic polarization in ferrimagnets, in contrast to multisublattice ferromagnets and antiferromagnets, where optical magnon modes residing in the THz regime are spin-unpolarized [1, 36, 39]. For out-of-plane magnetic anisotropy, as realized in Bi:YIG, the hybrid spectrum is fully gapped and all branches acquire nontrivial Chern numbers, signaling a topological phase. By contrast, for in-plane anisotropy, as realized in YIG, the gap closes when plasmon propagation is perpendicular to the magnetic ordering, and the corresponding hybrid modes exhibit Dirac-type crossings. These features are captured within the “effective Hamiltonian” framework developed here, which combines a macroscopic description of plasmons with microscopic response functions of the Rashba electron gas. Finally, we discuss experimentally accessible signatures of the hybridization, including topological interface states and an anomalous thermal Hall effect.

The remainder of the paper is organized as follows. In Sec. II A, we analyze the proximity effect involving a ferrimagnet with out-of-plane anisotropy, presenting the underlying model as well as both microscopic and macroscopic descriptions of the resulting hybrid plasmon-magnon modes and their topological classification. In Sec. II B, we extend this framework to the case of a ferrimagnet with in-plane anisotropy. Finally, Sec. III contains a discussion of the results and concluding remarks.

## II. HYBRID PLASMON-MAGNON MODES

### A. Out-of-plane magnetic ordering

Consider the interface between a monolayer semiconductor with broken inversion symmetry and an insulating ferrimagnet with out-of-plane magnetisation. The semiconductor hosts electrons with Rashba-type spin-orbit coupling, giving rise to collective plasmonic excitations that manifest as propagating coupled charge- and spin-density waves [40–43]. The ferrimagnet, in turn, supports propagating spin waves, or magnons. Direct plasmon-magnon coupling mediated by an oscillating magnetic field is relativistic in origin and therefore negligibly weak compared to the indirect exchange-mediated coupling

arising from interfacial interactions between the electron spins and local magnetic moments in the ferrimagnet.

For the sake of simplicity, we assume that the ferrimagnet has two sublattices and therefore supports a pair of magnon modes. In contrast to multisublattice ferromagnets and antiferromagnets, both branches  $\alpha = R/L$  carry uncompensated oscillating spin-polarisation,  $\ell^\alpha(\mathbf{r}, t)$ , which is perpendicular to the unit vector  $\mathbf{n} = e_z$  that aligns the out-of-plane spin ordering. After linearisation, the dynamics of both magnon branches become independent, and are governed by two independent Landau-Lifshitz-Gilbert (LLG) equations:

$$\rho_s (\alpha \partial_t [\ell^\alpha(\mathbf{r}, t) \times \mathbf{e}_z] - \omega_q^\alpha \ell^\alpha(\mathbf{r}, t)) = \Delta_\alpha \mathbf{s}(\mathbf{r}, t). \quad (1)$$

Here,  $\rho_s$  is the magnetic spin density, and  $\omega_q^\alpha$  is the dispersion of the magnon branches [44]. The coupling strength  $\Delta_\alpha$  between magnons and the electronic spin density  $\mathbf{s}(\mathbf{r}, t)$  is branch dependent, reflecting the different magnitudes and sign of the spin polarization carried by the two branches. As for plasmons, they manifest via oscillations of the scalar potential  $\phi(\mathbf{r}, t)$  generated by electron charge density oscillations  $\rho(\mathbf{r}, t)$  as

$$e\phi(\mathbf{r}, t) = \int d\mathbf{r}' V(\mathbf{r} - \mathbf{r}') \rho(\mathbf{r}, t). \quad (2)$$

Here,  $V(\mathbf{r}) = 2\pi/\kappa r$  is the electron-electron interaction and  $\kappa$  is the effective dielectric constant for the considered setup. Extension to a more complex dielectric or metallic gate-induced screening is straightforward.

The equations (1) and (2), which govern magnons and plasmons, are not directly coupled and remain independent until spin-orbit interactions entrain the charge- and spin-density dynamics of the electron gas in the monolayer semiconductor. Within a mean-field description, electrons interact both with the self-consistent macroscopic potential  $\phi(\mathbf{r}, t)$  and magnetic fluctuations  $\ell^\alpha(\mathbf{r}, t)$ , and their single-particle dynamics are described by the following Hamiltonian

$$\mathcal{H} = \frac{\mathbf{p}^2}{2m} + \alpha_R [\mathbf{p} \times \boldsymbol{\sigma}]_z + (\Delta_R - \Delta_L) \boldsymbol{\sigma} \cdot \mathbf{n} - \epsilon_F + \sum_\alpha \Delta_\alpha \boldsymbol{\sigma} \cdot \ell^\alpha(\mathbf{r}, t) + e\phi(\mathbf{r}, t). \quad (3)$$

Here  $m$  is the effective mass,  $\alpha_R$  is the Rashba coupling, and  $\epsilon_F$  is the Fermi level for electrons. The electron band dispersion of Rashba electrons,  $E^\sigma(\mathbf{p}) = \mathbf{p}^2/2m + \sigma \sqrt{\alpha_R^2 p^2 + (\Delta_R - \Delta_L)^2}$ , has two helicities  $\sigma = \uparrow / \downarrow$ , with electronic spin textures exhibiting opposite chiral windings. The two Rashba subbands have two different band-dependent Fermi momenta [45], given as

$$p_F^\sigma = \sqrt{2m\epsilon_F + (m\alpha_R)^2} - \sigma m\alpha_R. \quad (4)$$

Since the two ferrimagnetic modes couple to electrons in a similar way, we will present only the analysis of the coupling with the right-handed magnon mode, but include both chiralities in the plots presented below.

To obtain a closed set of equations, Eqs. (1) and (2) must be supplemented with the matter response. In this work we follow the hydrodynamic scheme to describe plasmons [46, 47], excluding electron density using the continuity equation

$$\partial_t \rho(\mathbf{r}, t) + \nabla \cdot \mathbf{j}(\mathbf{r}, t) = 0, \quad (5)$$

and calculate the linear response of electron spin  $\mathbf{s}(\mathbf{r}, t)$  and current  $\mathbf{j}(\mathbf{r}, t)$  densities using the Kubo theory [48]. In the local and the high-frequency approximations (See Appendix A for details) the response functions can be presented as

$$\begin{aligned} \mathbf{j}(\mathbf{r}, \omega) &= -\frac{e^2 v_F^2 N_F^+}{i\omega} \mathbf{E}(\mathbf{r}, \omega) + ev_F \Delta_\alpha N_F^- [\mathbf{e}_z \times \boldsymbol{\ell}^\alpha(\mathbf{r}, \omega)], \\ \mathbf{s}(\mathbf{r}, \omega) &= \Delta_\alpha N_F^+ \boldsymbol{\ell}^\alpha(\mathbf{r}, \omega) + \frac{ev_F N_F^-}{i\omega} [\mathbf{e}_z \times \mathbf{E}(\mathbf{r}, \omega)]. \end{aligned} \quad (6)$$

Where  $N_F^\pm = N_F^\uparrow \pm N_F^\downarrow = (p_F^\uparrow \pm p_F^\downarrow)/2\pi\hbar^2 v_F$  is the sum/difference of the Rashba subband's electronic density of states at the Fermi level and  $v_F$  is the Fermi velocity [49]. It should be noted that these expressions naturally capture the case with only one of two Rashba bands filled — one of  $N_F^{\uparrow/\downarrow}$  just vanishes. In the absence of spin-orbit interactions, i.e., when two subbands match and  $N_F^- = 0$ , all cross-correlated response functions vanish, such that plasmon and magnon oscillations decouple.

The conventional and shortest approach to calculate the dispersion of hybrid modes is to exclude all the fields except for the electric field, yielding a single equation in terms of the dielectric function  $\epsilon(\mathbf{q}, \omega) = 0$  that incorporates electron-magnon interactions. For a realistic set of parameters given in Sec. III, the dispersion of hybrid modes is presented in Fig. (2a). Plasmons interact effectively with both left- and right-handed magnon modes, spanning the GHz and THz frequency ranges. As is evident, the coupling to the optical mode is stronger than the acoustic one. Although the conventional approach successfully describes the dispersion relations of the hybrid modes, it overlooks their nontrivial topological character.

The nontrivial topological features become apparent only when the set of equations, Eqs (1-6), are reformulated in terms of an effective Hamiltonian, following the framework developed to describe plasmons in 2D and 3D electron gases [50–53], as well as other physical systems [54–57]. If we exclude the spin density and electric fields and rescale the field describing magnetic fluctuations,  $\zeta^\alpha(\mathbf{q}, \omega) = \sqrt{g_\alpha/\bar{\omega}_\mathbf{q}^\alpha} ev_F \Delta_\alpha N_F^- \boldsymbol{\ell}^\alpha(\mathbf{q}, \omega)$ , the corresponding equations can be presented as an eigenvalue problem  $\Omega \psi(\mathbf{q}, \omega) = \hat{\mathcal{H}}_{p-m}(\mathbf{q}) \psi(\mathbf{q}, \omega)$ . Here, the 5-component vector  $\psi(\mathbf{q}, \omega) = \{\zeta_x^\alpha(\mathbf{q}, \omega), \zeta_y^\alpha(\mathbf{q}, \omega), j_x(\mathbf{q}, \omega), \omega_p(\mathbf{q})\rho(\mathbf{q}, \omega)/q, j_y(\mathbf{q}, \omega)\}$  serves as the state vector, and the Hermitian matrix  $\hat{\mathcal{H}}_{p-m}$  can be interpreted as the “effective Hamiltonian”

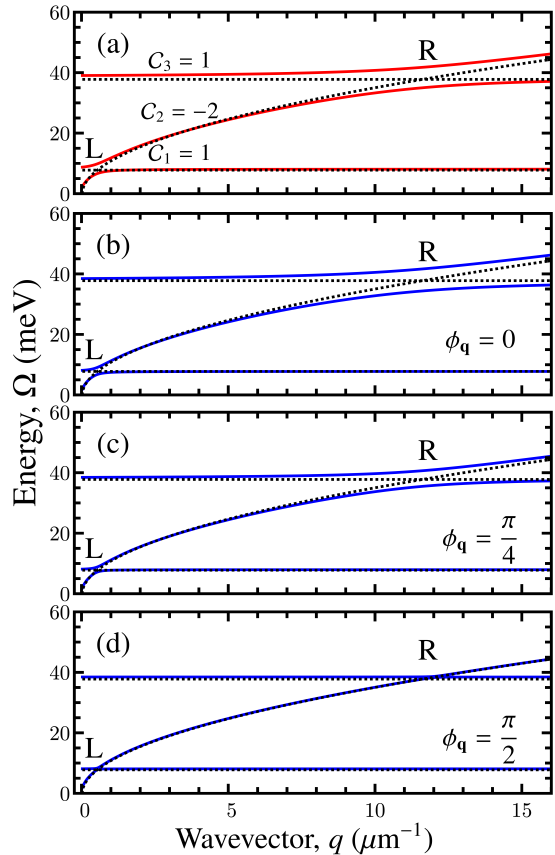


FIG. 2. Dispersion of hybrid plasmon-magnon modes (red or blue), shown together with the corresponding bare plasmon and magnon branches (dashed). (a) For *out-of-plane magnetic ordering*, the hybrid modes acquire a nontrivial topological character, with each branch carrying a nonzero Chern number (see insets). For *in-plane magnetic ordering*, the hybridization depends on the relative angle between the propagation direction and the magnetization axis,  $\phi_\mathbf{q}$ , and vanishes for perpendicular orientation,  $\phi_\mathbf{q} = \pi/2$ , leading to Dirac-like branch crossings. In all panels, L (R) denotes left- (right-) handed magnon modes.

of the considered system and is given by

$$\mathcal{H}_\mathbf{q}^{\text{out}} = \begin{pmatrix} 0 & -i\bar{\omega}_\mathbf{q}^\alpha & 2iM_\mathbf{q}^\alpha & 0 & 0 \\ i\bar{\omega}_\mathbf{q}^\alpha & 0 & 0 & 0 & 2iM_\mathbf{q}^\alpha \\ -2iM_\mathbf{q}^\alpha & 0 & 0 & \omega_\mathbf{q}^p n_\mathbf{q}^x & -ig_\alpha \\ 0 & 0 & \omega_\mathbf{q}^p n_\mathbf{q}^x & 0 & \omega_\mathbf{q}^p n_\mathbf{q}^y \\ 0 & -2iM_\mathbf{q}^\alpha & ig_\alpha & \omega_\mathbf{q}^p n_\mathbf{q}^y & 0 \end{pmatrix}. \quad (7)$$

The bottom-right  $3 \times 3$  block describes plasmons in the absence of magnons. Here,  $\omega_\mathbf{q}^p = v_F \sqrt{\alpha_{\text{eff}} k_F q}$  is the bare plasmon dispersion with  $\alpha_{\text{eff}} = \alpha_{\text{vac}} c / \kappa v_F$  being the modified fine-structure constant and  $\alpha_{\text{vac}}$  being the vacuum fine-structure constant.  $n_\mathbf{q} = \{\cos(\phi_\mathbf{q}), \sin(\phi_\mathbf{q})\}$  denotes its direction of plasmon propagation. The frequency  $g_\alpha = \alpha_R^2 \Delta_\alpha^2 N_F^+ / v_F^2 \rho_S$  quantifies the strength of plasmon coupling to magnetic moments across the interface. Mimicking the effect of an out-of-plane magnetic field, this coupling opens a gap in the plasmon spectrum,  $\bar{\omega}_\mathbf{q}^p = \sqrt{(\omega_\mathbf{q}^p)^2 + g_\alpha^2}$ . For realistic material parameters,

however, this gap remains small and is barely discernible in Fig. (2).

The top-right  $2 \times 2$  block describes magnons in the absence of plasmons. Exchange interactions with the electronic spins across the interface renormalize the magnon dispersion,  $\bar{\omega}_{\mathbf{q}}^{\alpha} = \omega_{\mathbf{q}}^{\alpha} + g_{\alpha}(v_F^2/\alpha_R^2 - 1)$  thereby shifting it to higher frequencies.

The off-diagonal  $2 \times 3$  and  $3 \times 2$  blocks describe the plasmon-magnon coupling. Its matrix structure can be understood as follows: according to the LLG equation, the dynamics of one component of the magnetic fluctuations, i.e.  $\ell_x(\mathbf{r}, t)$ , is governed by the spin polarization perpendicular to it,  $\dot{\ell}_x(\mathbf{r}, t) = \Delta s_y(\mathbf{r}, t)/\rho_s$ . For a Rashba electronic spectrum, the spin density  $s_y(\mathbf{r}, t)$  accompanies the charge current  $j_x(\mathbf{r}, t)$  and therefore enforces a component-resolved coupling  $\ell_x \leftrightarrow j_x$  (and analogously  $\ell_y \leftrightarrow j_y$ ). The coupling matrix element  $M_{\mathbf{q}}^{\alpha} = \sqrt{g_{\alpha}\bar{\omega}_{\mathbf{q}}^{\alpha}}/2$  depends not only on the coupling frequency  $g_{\alpha}$  but also explicitly on the magnon frequency. As a consequence, the plasmon-magnon coupling is stronger for the high-frequency magnon branch than for the low-energy branch, in agreement with Fig. (2).

The effective Hamiltonian  $\mathcal{H}_{\mathbf{q}}^{\text{out}}$  contains the complete information about the dispersion of the hybrid plasmon-magnon modes and their topologies. The dispersion relations are given by the positive frequency eigenvalues of the effective Hamiltonian [58] and are given by

$$\Omega_{\mathbf{q}}^{\pm} = \frac{\tilde{\omega}_{\mathbf{q}}^{\text{p}} + \bar{\omega}_{\mathbf{q}}^{\alpha}}{2} \pm \sqrt{\left(\frac{\tilde{\omega}_{\mathbf{q}}^{\text{p}} - \bar{\omega}_{\mathbf{q}}^{\alpha}}{2}\right)^2 + (M_{\mathbf{q}}^{\alpha})^2}, \quad (8)$$

and is presented in Fig. (2) [59]. The three hybrid branches can be labeled by index  $n = 1, 2, 3$  and their topology is characterized by the Chern numbers

$$\mathcal{C}_n = \int \frac{d\mathbf{q}}{2\pi} \mathcal{B}_n(\mathbf{q}), \quad \mathcal{B}_n(\mathbf{q}) = \nabla_{\mathbf{q}} \times \mathcal{A}_n(\mathbf{q}) \quad (9)$$

Here we introduce the Berry curvature  $\mathcal{B}_n(\mathbf{q})$ , defined via the Berry connection  $\mathcal{A}_n(\mathbf{q}) = \langle \mathbf{u}_{\mathbf{q}}^n | i\nabla_{\mathbf{q}} | \mathbf{u}_{\mathbf{q}}^n \rangle$ , where  $|\mathbf{u}_{\mathbf{q}}^n\rangle$  denotes the corresponding eigenvector. As shown in Fig. (2), the set of Chern numbers  $\mathcal{C} = \{1, -2, 1\}$  is nonzero, reflecting nontrivial topologies of the hybrid modes. We defer the discussion of possible manifestations of these topologies to Sec. III and instead focus on how the nontrivial topologies emerge.

The interaction-induced mixing between plasmons and magnons is most pronounced in the vicinity of the avoided crossings, where it can be accurately described by effective  $2 \times 2$  Hamiltonians obtained by projecting the full Hamiltonian onto a pair of the interacting modes. Its explicit expression

$$\bar{\mathcal{H}}_{\mathbf{q}}^{\text{out}} = \begin{pmatrix} \bar{\omega}_{\mathbf{q}}^{\text{p}} & M_{\mathbf{q}}^{\alpha} e^{\alpha i \phi_{\mathbf{q}}} \\ M_{\mathbf{q}}^{\alpha} e^{-\alpha i \phi_{\mathbf{q}}} & \bar{\omega}_{\mathbf{q}}^{\alpha} \end{pmatrix}. \quad (10)$$

confirms the interpretation of  $M_{\mathbf{q}}^{\alpha}$  as the magnitude of the matrix element governing plasmon-magnon coupling. The Hamiltonian  $\bar{\mathcal{H}}_{\mathbf{q}}^{\text{out}}$  constitutes a canonical minimal

model of a band-inversion-driven topological transition, featuring handedness-dependent phase winding factors. The intertwining of plasmons with right- and left-handed modes endows the resulting hybrid bands with Chern numbers  $\mathcal{C}_R = \{1, -1, 0\}$  and  $\mathcal{C}_L = \{0, -1, 1\}$ , respectively. Taken together, these contributions reproduce the result given for  $\mathcal{C}$  presented above.

Typically, a  $2 \times 2$  Hamiltonian associated with  $\bar{\mathcal{H}}_{\mathbf{q}}^{\text{out}}$  describes the hybridization between an  $s$ -wave-like band and an opposite-parity band of  $p_x \pm ip_y$  symmetry. Such a structure is characteristic of band inversion problems underlying topological phase transitions. In the present setting, the role of the chiral  $p_x \pm ip_y$  branch is played by magnons: the circular precession of localized spins endows them with a helicity-dependent orbital character. The longitudinal plasmon mode, by contrast, is even under parity and therefore serves as the effective  $s$ -wave sector of the hybridized system.

## B. In-plane magnetic ordering

The framework developed above can be straightforwardly extended to ferrimagnets with in-plane anisotropy. Without loss of generality, we take the equilibrium spin-ordering direction, represented by the unit vector  $\mathbf{n}$ , to lie along the  $y$  axis. Magnetization fluctuations, described by  $\ell = (\ell_x, 0, \ell_z)$ , then involve both in-plane and out-of-plane components, whose physical roles are not equivalent.

Unless the Fermi energy is extremely small — which is unfavorable for plasmons — the out-of-plane component of the electronic spin near the Fermi level is not only weak in magnitude but also aligned in the same direction across the entire Fermi contour in both bands. As a result, uniform plasmon-induced current oscillations do not produce an out-of-plane spin-density response, and the coupling to the  $\ell_z$  component of magnetic fluctuations is therefore suppressed in the long-wavelength limit. The plasmon-magnon interaction is thus mediated only via the linear response of the in-plane component of the magnetic fluctuations  $\ell_x$  to the corresponding electronic spin-density component  $s_x$ .

The extension of the effective Hamiltonian framework for in-plane magnetic ordering of ferrimagnets is presented in Appendix B. It can be characterized by the effective Hamiltonian acting at the 5-component vector  $\psi(\mathbf{q}, \omega) = \{\zeta_x(\mathbf{q}, \omega), \zeta_z(\mathbf{q}, \omega), j_z(\mathbf{q}, \omega), \omega_p(\mathbf{q})\rho(\mathbf{q}, \omega)/q, j_y(\mathbf{q}, \omega)\}$  and given by

$$\mathcal{H}_{\mathbf{q}}^{\text{in}} = \begin{pmatrix} 0 & -i\bar{\omega}_{\mathbf{q}}^{\alpha} & 0 & 0 & 0 \\ i\bar{\omega}_{\mathbf{q}}^{\alpha} & 0 & 0 & 0 & 2iM_{\mathbf{q}}^{\alpha} \\ 0 & 0 & 0 & \omega_{\mathbf{q}}^{\text{p}} n_{\mathbf{q}}^x & 0 \\ 0 & 0 & \omega_{\mathbf{q}}^{\text{p}} n_{\mathbf{q}}^x & 0 & \omega_{\mathbf{q}}^{\text{p}} n_{\mathbf{q}}^y \\ 0 & -2iM_{\mathbf{q}}^{\alpha} & 0 & \omega_{\mathbf{q}}^{\text{p}} n_{\mathbf{q}}^y & 0 \end{pmatrix}. \quad (11)$$

It has the same mathematical structure as  $\bar{\mathcal{H}}_{\mathbf{q}}^{\text{out}}$ , but only the coupling  $\ell_z \leftrightarrow j_y$  is involved, and the dispersion rela-

tion of plasmons is not renormalized by interactions with spins across the interface. We use the same set of parameters for plotting, and the resulting dispersion relations of the hybrid modes are shown in Fig. 2(b-d). In contrast to the case of out-of-plane magnetic ordering, the spectra are strongly anisotropic and exhibit the same angular dependence for both magnon branches. The plasmon-magnon coupling is maximized when the plasmon propagates parallel to the magnetic ordering, and vanishes for perpendicular propagation, where the plasmon-induced spin-density modulation is orthogonal to the magnetic fluctuations. This angular dependence can be made explicit by projecting the full Hamiltonian onto the pair of interacting hybrid modes, yielding

$$\bar{\mathcal{H}}_{\mathbf{q}}^{\text{in}} = \begin{pmatrix} \bar{\omega}_{\mathbf{q}}^{\text{p}} & M_{\mathbf{q}}^{\alpha} \cos(\phi_{\mathbf{q}}) \\ M_{\mathbf{q}}^{\alpha} \cos(\phi_{\mathbf{q}}) & \bar{\omega}_{\mathbf{q}}^{\alpha} \end{pmatrix}. \quad (12)$$

The angular dependence of the matrix element  $M_{\mathbf{q}}^{\alpha} \cos \phi_{\mathbf{q}}$  exhibits  $p$ -wave symmetry and vanishes at  $\phi_{\mathbf{q}} = \pm\pi/2$ . In the vicinity of the branch-touching points, the effective Hamiltonian can be linearized as  $\bar{\mathcal{H}}_{\mathbf{q}}^{\text{out}} = \epsilon_0 \pm v_x(\hat{q}_x - q_0)(\hat{1} + \hat{\sigma}_z)/2 + v_y \hat{q}_y$ , revealing the Dirac-like nature of the branch crossings. It should be noted, however, that the emergent Dirac points in this case are not symmetry-protected, and a gap may in principle open if additional coupling mechanisms or previously neglected terms are incorporated [60]. All these effects, however, are small for the setup considered here, thereby favoring a strongly anisotropic hybridization of the resulting modes.

### III. DISCUSSIONS

Owing to the hybrid nature of the modes, the avoided crossing can be accessed through either their plasmonic or magnonic components. In particular, the plasmonic sector can be probed using scattering-type near-field optical microscopy (s-SNOM), as well as other related near-field techniques [31, 61, 62], or through electron energy-loss spectroscopy [63, 64]. Conversely, probing the magnonic sector — for example via inelastic neutron scattering — will reveal the same avoided-crossing structure in the magnon spectrum, reflecting the underlying hybridization of the modes [65, 66].

A hallmark of nontrivial topology is the existence of robust, topologically protected edge modes at interfaces between regions characterized by different Chern numbers. Reversing the direction of the equilibrium out-of-plane magnetization ( $\mathbf{e}_z \rightarrow -\mathbf{e}_z$ ) in a ferrimagnet reverses the precession of magnetic moments and inverts the Chern numbers of all three hybrid branches ( $\mathcal{C} \rightarrow -\mathcal{C}$ ). Consequently, a magnetic domain wall separating regions with opposite magnetization is expected to host protected hybrid plasmon-magnon edge modes.

The emergence of topological magnon-plasmon modes is accompanied by a sizable Berry curvature across all three hybrid branches. The Berry curvature is strongly

concentrated near the avoided crossings and can give rise to a pronounced anomalous thermal Hall response [67]. Similar effects have been discussed for hybrid phonon-magnon systems [25, 26]. Experimental observation of such a thermal Hall signal would therefore provide a clear signature of the formation of topological hybrid modes.

For material estimates, the magnonic sector parameters are relevant to the  $\text{YiG}$  ferrimagnetic insulator [36]: We approximate the bare magnon dispersion to be flat and given by  $\bar{\omega}_{\mathbf{q}}^{\text{R(L)}} \approx 38 \text{ meV}$  (8 meV), a density of magnetic spins of  $\rho_{\text{S}} \approx 2 \times 10^{12} \text{ cm}^{-2}$ , and an effective exchange interaction of  $\Delta_{\text{R(L)}} = 70 \text{ meV}$  (50 meV) (See App. C for details). The electron sector parameters are relevant to the Janus two-dimensional dichalcogenide  $\text{SMoSe}$  [33]: electron doping of  $n_{\text{e}} \approx 2.5 \times 10^{12} \text{ cm}^{-2}$ , a Rashba coupling strength of  $\alpha_{\text{R}} = 1.5 \times 10^{-5} \text{ meV cm}$ , an effective electron mass of  $m = 0.05m_0$ , where  $m_0$  is the electron rest mass, and a relative dielectric constant of  $\kappa = 3$ .

Employing ferrimagnets in magnetic heterostructures enhances the magnon-plasmon coupling strength, which can be seen by calculating the coupling matrix elements. With parameters stated above, the resulting matrix elements are given by  $M_{\mathbf{q}}^{\text{R}} \approx 3.64 \text{ meV}$  and  $M_{\mathbf{q}}^{\text{L}} \approx 1.20 \text{ meV}$ , showing that the coupling with the high-frequency THz magnon mode is strongly enhanced compared to that of the lower frequency mode, which is evident in Fig. (2). This enhancement is due to a combination of the magnon energy dependence ( $\propto \sqrt{\bar{\omega}_{\mathbf{q}}^{\alpha}}$ ) of the matrix elements, which favors the higher frequency magnon mode, and the s-d(f) onsite exchange interaction between electron and magnetic spin becoming enhanced by a factor dependent on the Bogoliubov coefficients (see App. C for the microscopic derivation). The latter is a feature that ferrimagnets share with antiferromagnets [15, 68], but is distinguished from antiferromagnets by an inherent broken degeneracy between the magnon chiralities that pushes the upper magnon mode into the THz frequency range, which is favorable for plasmonic experiments. The enhanced coupling also enables access to the strong-hybridisation regime in which the hybridization gap exceeds plasmonic spectral broadening induced by dissipative processes such as Landau damping and impurity scattering [29, 30]. Thus, ferrimagnet-based magnetic heterostructures provide a readily accessible experimental platform for investigating plasmon-magnon hybridization, which has not yet been experimentally demonstrated.

To conclude, by combining microscopic and macroscopic descriptions of magnon-plasmon coupling, we demonstrate that plasmons and magnons undergo strong hybridization at the interface between a Janus TMD and an insulating two-sublattice ferrimagnet, spanning both the GHz and THz frequency regimes. Moreover, the developed framework provides a natural and efficient classification of the topology of the hybrid modes, which originates from the phase winding of the magnon-plasmon coupling induced by spin-momentum locking and the accompanying chiral winding of the electronic spin along

the Fermi contours.

## ACKNOWLEDGEMENTS

We acknowledge fruitful discussions with Michael Fuhrer, Haoran Ren, and Michail Glazov, as well as support from the Australian Research Council Centre of Excellence in Future Low-Energy Electronics Technologies (CE170100039).

## Appendix A: Microscopically evaluated response functions

This Appendix presents a microscopic derivation of the expression Eq. (6) from the main text. The Rashba electrons can be described by the following Hamiltonian

$$\mathcal{H}_0 = \frac{\mathbf{p}^2}{2m_*} + \alpha_R [\mathbf{p} \times \boldsymbol{\sigma}]_z + \Delta\sigma_z, \quad (\text{A1})$$

Here  $m_*$  is the effective electron band mass,  $\alpha_R$  is the Rashba coupling, and  $\Delta$  is the exchange energy from the coupling with the Ferrimagnet. We note that the magnetic exchange interaction term in Eq. (A1) implies the magnetisation axis to be pointing in the  $z$ -direction. This does not lose any generality with the calculation of the response functions, and it is easy to generalise the following calculations to the in-plane magnetisation axis case. The electron dispersion from this Hamiltonian is given as  $\epsilon_{\mathbf{p}}^{\sigma} = \frac{\mathbf{p}^2}{2m_*} + \sigma\epsilon_{\mathbf{p}}^{\alpha_R}$ ,  $\epsilon_{\mathbf{p}}^{\alpha_R} = \sqrt{\alpha_R^2 p^2 + \Delta^2}$  is the spin-orbit interaction energy, and  $\sigma = \uparrow / \downarrow$  indexes the Rashba subbands with opposite spin polarisation. The spinor wavefunctions of this Hamiltonian are given as

$$|\uparrow, \mathbf{p}\rangle = \begin{pmatrix} \cos(\frac{\theta}{2}) \\ i \sin(\frac{\theta}{2}) e^{i\phi_{\mathbf{p}}} \end{pmatrix}, \quad |\downarrow, \mathbf{p}\rangle = \begin{pmatrix} \sin(\frac{\theta}{2}) \\ -i \cos(\frac{\theta}{2}) e^{i\phi_{\mathbf{p}}} \end{pmatrix}. \quad (\text{A2})$$

Here  $\phi_{\mathbf{p}}$  is the polar angle for the momentum  $\mathbf{p}$  and  $\cos(\theta) = \Delta/\epsilon_{\mathbf{p}}^{\alpha_R}$  is the out-of-plane spin component. The calculation of the susceptibilities is essentially the calculation of the corresponding spin-current polarisation bubbles. First we note that the spin and current operators of the Hamiltonian Eq. (A1) are given by  $\hat{j} = \frac{e}{m_*} \hat{\mathbf{p}} + e\alpha_R [\boldsymbol{\sigma} \times \mathbf{e}_z]$ , and  $\hat{s} = [\boldsymbol{\sigma} \times \mathbf{e}_z]$ . We thus can express the linear response of the current and density fields as the following

$$\begin{aligned} \mathbf{j}(\mathbf{r}, \omega) &= \hat{\sigma}(\omega) \mathbf{E}(\mathbf{r}, \omega) + \hat{\chi}(\omega) [\mathbf{e}_z \times \boldsymbol{\ell}(\mathbf{r}, \omega)], \\ \mathbf{s}(\mathbf{r}, \omega) &= \hat{\kappa}(\omega) \boldsymbol{\ell}(\mathbf{r}, \omega) + \hat{\Lambda}(\omega) [\mathbf{e}_z \times \mathbf{E}(\mathbf{r}, \omega)]. \end{aligned} \quad (\text{A3})$$

Fig. (3) shows the relevant Feynmann diagrams needed to calculate the response functions. Starting with the AC conductivity, we note that as there are no external magnetic fields, the conductivity tensor is diagonal with only the longitudinal conductivity being non-zero,  $\hat{\sigma}(\omega) = \sigma_{xx}(\omega)$ . The AC conductivity is directly proportional to the density-density response function and thus

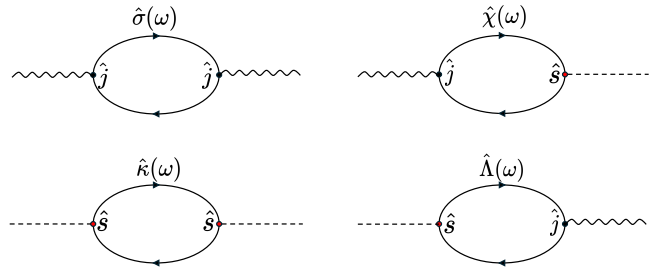


FIG. 3. Feynmann diagrams of the response functions in Eq. (A3). The solid arrowed lines represent the non-interacting retarded electron Greens function  $G_{\sigma}^{(0)}(\mathbf{q}, \omega) = (\omega - \epsilon_{\mathbf{p}}^{\sigma} + i\delta)^{-1}$ , the dashed line represents the complex free magnon propagator  $D^{(0)}(\mathbf{q}, \omega) = -2\epsilon_{\mathbf{q}}/((\omega + i\delta)^2 + \epsilon_{\mathbf{q}}^2)$ , and the wiggly line represents the free plasmon field. Counter-clockwise from the top left:  $\hat{\sigma}(\omega)$  is the AC conductivity given by the electron current-current correlation function.  $\hat{\chi}(\omega)$  is the response function which encodes the current response from the magnetic spin fluctuation, given by the electron current-spin correlation function.  $\hat{\kappa}(\omega)$  is the response function which encodes the electron spin-density response to the magnetic spin fluctuation, given by the spin-spin correlation function.  $\hat{\Lambda}(\omega)$  is the response function which encodes the spin-density response to the internal self consistent electric field from the electron density fluctuations, given by the spin-current correlation function.

can be calculated in the RPA using the formalism developed in [69–71] as

$$\sigma_{xx} = \frac{i}{\omega} \sum_{\mathbf{p}, \sigma} |\langle \mathbf{p} + \mathbf{q}, \sigma | \hat{j}_x | \mathbf{p}, \sigma \rangle|^2 \mathcal{Z} \quad (\text{A4})$$

Here, we have introduced a compact notation

$$\mathcal{Z} = \frac{n_F(\epsilon_{\mathbf{p}+\mathbf{q}}^{\sigma}) - n_F(\epsilon_{\mathbf{p}}^{\sigma})}{\omega + \epsilon_{\mathbf{p}+\mathbf{q}}^{\sigma} - \epsilon_{\mathbf{p}}^{\sigma} + i\delta} \quad (\text{A5})$$

Furthermore we have neglected interband particle-hole excitations as for small momenta they become negligibly small [40]. Henceforth, all calculations will be performed in the limit  $q \ll p_F^{\sigma}$  and  $\omega \ll \epsilon_F$ . This allows the following simplifications

$$\begin{aligned} n_F(\epsilon_{\mathbf{p}+\mathbf{q}}^{\sigma}) - n_F(\epsilon_{\mathbf{p}}^{\sigma}) &= q \cos(\phi_{\mathbf{p}} - \phi_{\mathbf{q}}) \delta(p - p_F^{\sigma}), \\ \epsilon_{\mathbf{p}+\mathbf{q}}^{\sigma} - \epsilon_{\mathbf{p}}^{\sigma} &= v_F q \cos(\phi_{\mathbf{p}} - \phi_{\mathbf{q}}), \end{aligned} \quad (\text{A6})$$

where  $v_F = \frac{p_F^{\sigma}}{m_*} - \sigma\alpha_R = \sqrt{2m_*\epsilon_F + k_{\alpha_R}^2}$  is the Fermi velocity. With,  $\phi = \phi_{\mathbf{p}} - \phi_{\mathbf{q}}$ , these simplifications give the following form for the matrix elements,

$$\langle \mathbf{p} + \mathbf{q}, \sigma | \hat{j}_x | \mathbf{p}, \sigma \rangle = ev_F \cos(\phi). \quad (\text{A7})$$

The final simplification we make is that  $\omega \gg v_F q$ , i.e. the dispersion of hybrid modes is far away from the intraband continuum of particle hole excitations. This is valid because the energy at which the magnon and plasmon branches cross is far away from the particle hole

continuum, and thus the essential physics is capture in the aforementioned limit. After this simplification, and upon performing the momentum integration we are left with the following form of the AC conductivity

$$\sigma_{xx}(\omega) = -\frac{e^2 v_F^2 N_F^+}{i\omega} \quad (\text{A8})$$

The calculation of the other susceptibilities proceeds in a near identical manner, with the following definitions of each susceptibility tensor

$$\begin{aligned} \hat{\kappa}(\omega) &= \Delta \sum_{\mathbf{p}, \sigma} |\langle \mathbf{p} + \mathbf{q}, \sigma | \hat{s}_i | \mathbf{p}, \sigma \rangle|^2 \mathcal{Z} \\ \hat{\Lambda}(\omega) &= \frac{i}{\omega} \sum_{\mathbf{p}, \sigma} \langle \mathbf{p} + \mathbf{q}, \sigma | \hat{s}_i | \mathbf{p}, \sigma \rangle \langle \mathbf{p}, \sigma | \hat{j}_j | \mathbf{p} + \mathbf{q}, \sigma \rangle \mathcal{Z}, \\ \hat{\chi}(\omega) &= \Delta \sum_{\mathbf{p}, \sigma} \langle \mathbf{p} + \mathbf{q}, \sigma | \hat{j}_i | \mathbf{p}, \sigma \rangle \langle \mathbf{p}, \sigma | \hat{s}_j | \mathbf{p} + \mathbf{q}, \sigma \rangle \mathcal{Z} \end{aligned} \quad (\text{A9})$$

and The final forms of all these susceptibility tensors is stated in Eq. (6).

## Appendix B: Extension of the framework to the in-plane magnetic ordering

This Appendix presents the eigenvalue reformulation of the LLG equations to the in-plane easy axis anisotropy case. Focusing on a single magnon branch, we can express the LLG equation as follows

$$\begin{aligned} \omega \ell^\alpha(\mathbf{r}, t) &= -i\omega_q^\alpha [\mathbf{e}_y \times \ell^\alpha(\mathbf{r}, t)] - \\ &\quad i \frac{\Delta_\alpha}{\rho_S} [\mathbf{e}_y \times \mathbf{s}(\mathbf{r}, t)], \end{aligned} \quad (\text{B1})$$

where, without loss of generality, we chose a magnetization axis of  $\mathbf{n} = \mathbf{e}_y$ . The difference in sign as compared to the out-of-plane LLG equation comes from the fact that we have performed an odd permutation of the basis vectors of the magnetisation vector, so the cross products pick up a negative sign as pseudovectors. Furthermore, the current and spin-density fields have the linear response relation.

$$\begin{aligned} \mathbf{j}(\mathbf{r}, \omega) &= -\frac{e^2 v_F^2 N_F^+}{i\omega} \mathbf{E}(\mathbf{r}, \omega) + ev_F \Delta_\alpha N_F^- \ell_x^\alpha(\mathbf{r}, t) \mathbf{e}_y \\ \mathbf{s}(\mathbf{r}, \omega) &= \Delta_\alpha N_F^+ \ell_x^\alpha(\mathbf{r}, \omega) \mathbf{e}_x + \frac{ev_F N_F^-}{i\omega} [\mathbf{e}_z \times \mathbf{E}(\mathbf{r}, \omega)]. \end{aligned} \quad (\text{B2})$$

By excluding the spin density and electric fields in Eq. (B1) using the linear response relations in Eq. (B2), the LLG equation takes the final form

$$\omega \zeta^\alpha(\mathbf{q}, \omega) = -i\bar{\omega}_q^\alpha [\mathbf{e}_y \times \zeta^\alpha(\mathbf{q}, \omega)] + 2iM_q^\alpha j_y(\mathbf{q}, \omega) \mathbf{e}_z, \quad (\text{B3})$$

where we have rescaled the magnetic fluctuation fields to have units of current density as  $\zeta^\alpha(\mathbf{q}, \omega) =$

$\sqrt{g_\alpha/\bar{\omega}_q^\alpha} ev_F \Delta_\alpha N_F^- \ell^\alpha(\mathbf{q}, \omega)$ . Finally, we can express the relations for the current and charge density fields by supplementing the expressions with the continuity equation, Eq. (5), which yields the Hamiltonian form of the expressions

$$\begin{aligned} \omega \mathbf{j}(\mathbf{q}, \omega) &= \omega_q^p \hat{\mathbf{n}}_q j_0(\mathbf{q}, \omega) - 2iM_q^\alpha \zeta_z^\alpha(\mathbf{q}, \omega) \mathbf{e}_y \\ j_0(\mathbf{q}, \omega) &= \omega_q^p \hat{\mathbf{n}}_q \cdot \mathbf{j}(\mathbf{q}, \omega), \end{aligned} \quad (\text{B4})$$

where  $j_0(\mathbf{q}, \omega) = \omega_q^p \rho(\mathbf{q}, \omega)/q$ . Thus, organizing Eqs. (B3) & (B4) into an eigenvalue problem, yields the effective Hamiltonian in Eq. (11)

## Appendix C: Microscopic derivation of Magnon spectrum and effective exchange interaction

In this appendix we derive the magnon dispersion from a minimal two-sublattice Heisenberg Hamiltonian and the effective exchange coupling of this magnet with electrons. For a two-sublattice Ferrimagnet there are two inequivalent spin sites that are anti-ferromagnetically coupled. Starting with the magnon dispersion, the Heisenberg Hamiltonian of such a system is given as

$$\mathcal{H}_s = J \sum_{\langle ij \rangle} \mathbf{S}_{i,A} \cdot \mathbf{S}_{j,B}, \quad (\text{C1})$$

where  $|\mathbf{S}_A| \neq |\mathbf{S}_B|$ . To diagonalise this Hamiltonian we can rotate one of the spin-sublattice sites by a  $\pi$  rotation, such that the ground-state appears Ferromagnetic [72]. The tradeoff in doing so is introducing particle non-conserving terms like  $\hat{b}\hat{b}$ . After performing this rotation and doing a Holstein-Primakoff transformation [73], we arrive at the intermediate form of the Hamiltonian as

$$\mathcal{H}_s = \sum_{\mathbf{q}} \Phi_{\mathbf{q}}^\dagger H_{\mathbf{q}} \Phi_{\mathbf{q}}, \quad (\text{C2})$$

here  $\Phi_{\mathbf{q}} = (a_{\mathbf{q}}, b_{-\mathbf{q}}^\dagger)$  is a spinor of magnon creation/annihilation operators on each spin-sublattice site in reciprocal space, and the Bloch Hamiltonian takes the form

$$H_{\mathbf{q}} = 4J \begin{pmatrix} S_B & \sqrt{S_A S_B} \gamma_{\mathbf{q}} \\ \sqrt{S_A S_B} \gamma_{\mathbf{q}} & S_A \end{pmatrix}, \quad (\text{C3})$$

where  $\gamma_{\mathbf{q}} = \frac{1}{2} [\cos(q_x/2) + \cos(q_y/2)]$  is the geometric factor of the lattice, which we have chosen to be a square lattice for simplicity. To diagonalise the Hamiltonian above, we perform a Bogoliubov transformation of the operators as

$$\begin{aligned} a_{\mathbf{q}} &= u_{\mathbf{q}} \xi_{\mathbf{q},R} + v_{\mathbf{q}} \xi_{\mathbf{q},L}^\dagger, \\ b_{\mathbf{q}} &= u_{\mathbf{q}} \xi_{\mathbf{q},L} + v_{\mathbf{q}} \xi_{\mathbf{q},R}^\dagger. \end{aligned} \quad (\text{C4})$$

The parameterisation we choose is  $u_{\mathbf{k}} = \cosh(\theta_{\mathbf{k}})$  and  $v_{\mathbf{k}} = \sinh(\theta_{\mathbf{k}})$  with  $\tanh(2\theta_{\mathbf{k}}) = 2\sqrt{S_A S_B} \gamma_{\mathbf{k}}/(S_A + S_B)$ ,

this transformation diagonalises the Hamiltonian as

$$H'_{\mathbf{q}} = \begin{pmatrix} \omega_{\mathbf{q}}^R & 0 \\ 0 & -\omega_{\mathbf{q}}^L \end{pmatrix}, \quad (\text{C5})$$

where

$$\omega_{\mathbf{q}}^{R/L} = \sqrt{J^2(S_A + S_B)^2 - J^2 S_A S_B |\gamma_{\mathbf{q}}|^2} \pm J(S_A - S_B). \quad (\text{C6})$$

The Hamiltonian that describes the exchange interaction between electron spin  $\boldsymbol{\sigma} = (\sigma_x, \sigma_y)$  and magnetic sublattice spin is given as

$$\mathcal{H}_{e-s} = \sum_i \Delta_A \boldsymbol{\sigma} \cdot \mathbf{S}_{i,A} + \Delta_B \boldsymbol{\sigma} \cdot \mathbf{S}_{i,B}, \quad (\text{C7})$$

where  $\Delta_{A/B}$  are the sublattice onsite exchange energies. Upon performing the Holstein-Primakoff transformation and Fourier transforming, takes the form

$$\mathcal{H}_{e-s} = \sum_{\mathbf{q}} \sqrt{2S_A} \Delta_A (\sigma^- a_{\mathbf{q}} + \sigma^+ a_{\mathbf{q}}^\dagger) + \sqrt{2S_B} \Delta_B (\sigma^- b_{\mathbf{q}}^\dagger + \sigma^+ b_{\mathbf{q}}), \quad (\text{C8})$$

where  $\sigma^\pm = \frac{1}{2}(\sigma_x \pm i\sigma_y)$ . To get the final form of the exchange interactions, we need to perform the Bogoliubov transform used to diagonalise the Heisenberg Hamiltonian, Eq. C4. Upon doing so, the final form of the Hamil-

tonian is easily seen to be

$$\sum_{\mathbf{q}} \Delta_R (\sigma^- \xi_{\mathbf{q},R} + \sigma^+ \xi_{\mathbf{q},R}^\dagger) + \Delta_L (\sigma^- \xi_{\mathbf{q},L}^\dagger + \sigma^+ \xi_{\mathbf{q},L}), \quad (\text{C9})$$

where

$$\begin{aligned} \Delta^R &= (\sqrt{2S_A} u_{\mathbf{q}} \Delta_A + \sqrt{2S_B} v_{\mathbf{q}} \Delta_B), \\ \Delta^L &= (\sqrt{2S_A} v_{\mathbf{q}} \Delta_A + \sqrt{2S_B} u_{\mathbf{q}} \Delta_B), \end{aligned} \quad (\text{C10})$$

are the effective exchange energies.

#### Appendix D: Derivation of linearised Landau-Lifshitz-Gilbert equations

This section derives the linearised LLG equations describing the two magnon chiralities presented in the main text. Consider a two sublattice ferrimagnet, the dynamic of each sublattice magnetic moment follow a set of coupled Landau-Lifshitz-Gilbert equations given as

$$\rho_S \partial_t \mathbf{n}^\alpha(\mathbf{r}, t) = [\mathbf{B}_{\text{Eff}}^\alpha \times \mathbf{n}^\alpha(\mathbf{r}, t)], \quad (\text{D1})$$

here we have assumed that the number density of magnetic spins of each sublattice are equal. The effective magnetic field is given as the energy conjugate of the potential energy  $\mathbf{B}_{\text{Eff}}^\alpha = -\delta U_{\mathbf{n}} / \delta \mathbf{n}^\alpha$  which is given as

$$U[\mathbf{n}_A, \mathbf{n}_B] = \int d\mathbf{r} \left\{ \rho_S \left[ J a^2 \nabla \mathbf{n}_A \cdot \nabla \mathbf{n}_B - \frac{\delta_s}{2} ((\mathbf{n}_A^\parallel)^2 + (\mathbf{n}_B^\parallel)^2) + 2J \mathbf{n}_A \cdot \mathbf{n}_B \right] + \Delta_A \mathbf{n}_A \cdot \mathbf{s} + \Delta_B \mathbf{n}_B \cdot \mathbf{s} \right\}, \quad (\text{D2})$$

where  $\mathbf{s}$  is the spin density as introduced in the main

text. Upon calculating the effective magnetic fields, we get the following coupled LLG equations

$$\begin{aligned} \rho_S \partial_t \mathbf{n}_A &= \rho_S J a^2 [\mathbf{n}_A \times \nabla^2 \mathbf{n}_B] + \rho_S 2J [\mathbf{n}_A \times \mathbf{n}_B] - \rho_S \delta_s [\mathbf{n}_A \times \boldsymbol{\ell}_A] + \Delta_A \mathbf{n}_A \times \mathbf{s}, \\ \rho_S \partial_t \mathbf{n}_B &= \rho_S J a^2 [\mathbf{n}_B \times \nabla^2 \mathbf{n}_A] + \rho_S 2J [\mathbf{n}_B \times \mathbf{n}_A] - \rho_S \delta_s [\mathbf{n}_B \times \boldsymbol{\ell}_B] + \Delta_B \mathbf{n}_B \times \mathbf{s}. \end{aligned} \quad (\text{D3})$$

Now we introduce the following order parameters, we linearise as  $\mathbf{n}_A = S_A (\mathbf{e}_z + \boldsymbol{\ell}_A)$  and  $\mathbf{n}_B = S_B (-\mathbf{e}_z + \boldsymbol{\ell}_B)$  which

yields, upon rearranging, the following linearised LLG equations

$$\begin{aligned} [\partial_t \boldsymbol{\ell}_A \times \mathbf{e}_z] - S_B J a^2 \nabla^2 \boldsymbol{\ell}_B - 2J S_B (\boldsymbol{\ell}_A + \boldsymbol{\ell}_B) + \delta_s S_A \boldsymbol{\ell}_A &= \frac{\Delta_A}{\rho_S} \mathbf{s}, \\ [\partial_t \boldsymbol{\ell}_B \times \mathbf{e}_z] + S_A J a^2 \nabla^2 \boldsymbol{\ell}_A + 2J S_A (\boldsymbol{\ell}_A + \boldsymbol{\ell}_B) - \delta_s S_B \boldsymbol{\ell}_B &= -\frac{\Delta_B}{\rho_S} \mathbf{s}. \end{aligned} \quad (\text{D4})$$

To de-couple these two equations, we can formulate the

set of coupled equations as a matrix equation with a

source term generated by the coupling with electron spin density written as  $(\hat{R}(\omega) + \hat{H}(\hat{\mathbf{p}}))|\ell\rangle = \frac{\Delta}{\rho_s}|\mathbf{s}\rangle$  where

$$\hat{R} = \begin{pmatrix} 0 & -i\omega & 0 & 0 \\ i\omega & 0 & 0 & 0 \\ 0 & 0 & 0 & -i\omega \\ 0 & 0 & i\omega & 0 \end{pmatrix}, \quad \hat{H} = \begin{pmatrix} S_A\delta_s - 2JS_B & 0 & Ja^2S_B\hat{p}_x^2 - 2JS_B & 0 \\ 0 & S_A\delta_s - 2JS_B & 0 & Ja^2S_B\hat{p}_y^2 - 2JS_B \\ -Ja^2S_A\hat{p}_x^2 + 2JS_A & 0 & -S_B\delta_s + 2JS_A & 0 \\ 0 & -Ja^2S_A\hat{p}_y^2 + 2JS_A & 0 & -S_B\delta_s + 2JS_A \end{pmatrix}. \quad (D5)$$

The momentum dependent matrix,  $\hat{H}$  is diagonalizable, and thus its Jordan normal form is diagonal with its eigenvalues on the diagonal. Assuming  $\delta_s = 0$  for simplicities sake, we diagonalise via the similarity transformation  $\hat{T}^{-1}\hat{H}(\mathbf{p})\hat{T} = \hat{D}$  where  $\hat{T}$  is the transition matrix who's columns are the eigenvectors of  $\hat{H}$ , yields the diagonal matrix

$$\hat{D} = \begin{pmatrix} \omega_{\mathbf{p}}^R & 0 & 0 & 0 \\ 0 & \omega_{\mathbf{p}}^R & 0 & 0 \\ 0 & 0 & -\omega_{\mathbf{p}}^L & 0 \\ 0 & 0 & 0 & -\omega_{\mathbf{p}}^L \end{pmatrix}, \quad (D6)$$

where  $\omega_{\mathbf{p}}^{R/L}$  is the same spectrum derived from the Heisenberg Hamiltonian, Eq. (C6). The form of the diagonal matrix is exactly identical to the diagonalised

we represent the kets in the cartesian basis as  $|\ell\rangle \rightarrow (\ell_A^x, \ell_A^y, \ell_B^x, \ell_B^y)$ ,  $|\mathbf{s}\rangle \rightarrow (s^x, s^y, s^x, s^y)$  and

$$\hat{R}(\omega)\hat{T}^{-1}|\ell\rangle + \hat{D}(\mathbf{p})\hat{T}^{-1}|\ell\rangle = \frac{\Delta}{\rho_s}\hat{T}^{-1}|\mathbf{s}\rangle, \quad (D7)$$

Heisenberg Hamiltonian after performing a Bogoliubov transformation, indicating that the diagonalisation above is equivalent to the Bogoliubov transformation. Furthermore because this matrix is diagonalised, it is easy to see that we can present the equations as

$$\rho_s(\partial_t[\ell^R(\mathbf{r}, t) \times \mathbf{e}_z] - \omega_q^R\ell^R(\mathbf{r}, t)) = \Delta_R\mathbf{s}(\mathbf{r}, t), \quad (D8)$$

$$\rho_s(\partial_t[\mathbf{e}_z \times \ell^L(\mathbf{r}, t)] - \omega_q^L\ell^L(\mathbf{r}, t)) = \Delta_L\mathbf{s}(\mathbf{r}, t), \quad (D8)$$

where now  $\ell^R = \sum_j(T_{1j}^{-1}|\ell\rangle_j, T_{2j}^{-1}|\ell\rangle_j)$  and  $\ell^L = \sum_j(T_{3j}^{-1}|\ell\rangle_j, T_{4j}^{-1}|\ell\rangle_j)$

- [1] Se Kwon Kim, Geoffrey S. D. Beach, Kyung-Jin Lee, Teruo Ono, Theo Rasing, and Hyunsoo Yang, “Ferrimagnetic spintronics,” *Nature Materials* **21**, 24–34 (2022).
- [2] Sasikanth Manipatruni, Dmitri E. Nikonorov, and Ian A. Young, “Beyond cmos computing with spin and polarization,” *Nature Physics* **14**, 338–343 (2018).
- [3] Semonti Bhattacharyya, Golrokh Akhgar, Matthew Gebert, Julie Karel, Mark T. Edmonds, and Michael S. Fuhrer, “Recent Progress in Proximity Coupling of Magnetism to Topological Insulators,” *Advanced Materials* **33**, 2007795 (2021).
- [4] Arne Brataas, Andrew D. Kent, and Hideo Ohno, “Current-induced torques in magnetic materials,” *Nature Materials* **11**, 372–381 (2012).
- [5] H. Nakayama, M. Althammer, Y.-T. Chen, K. Uchida, Y. Kajiwara, D. Kikuchi, T. Ohtani, S. Geprägs, M. Opel, S. Takahashi, R. Gross, G. E. W. Bauer, S. T. B. Goennenwein, and E. Saitoh, “Spin hall magnetoresistance induced by a nonequilibrium proximity effect,” *Phys. Rev. Lett.* **110**, 206601 (2013).
- [6] Cui-Zu Chang, Jinsong Zhang, Xiao Feng, Jie Shen, Zuocheng Zhang, Minghua Guo, Kang Li, Yunbo Ou, Pang Wei, Li-Li Wang, Zhong-Qing Ji, Yang Feng, Shuaihua Ji, Xi Chen, Jinfeng Jia, Xi Dai, Zhong Fang, Shou-Cheng Zhang, Ke He, Yayu Wang, Li Lu, Xu-Cun Ma, and Qi-Kun Xue, “Experimental observation of the quantum anomalous hall effect in a magnetic topological insulator,” *Science* **340**, 167–170 (2013).
- [7] Mehdi Kargarian, Dmitry K. Efimkin, and Victor Galitski, “Amperean pairing at the surface of topological insulators,” *Phys. Rev. Lett.* **117**, 076806 (2016).
- [8] Eirik Erlandsen, Arne Brataas, and Asle Sudbø, “Magnon-mediated superconductivity on the surface of a topological insulator,” *Phys. Rev. B* **101**, 094503 (2020).
- [9] Even Thingstad, Eirik Erlandsen, and Asle Sudbø, “Eliashberg study of superconductivity induced by interfacial coupling to antiferromagnets,” *Phys. Rev. B* **104**, 014508 (2021).
- [10] Kristian Mæland and Asle Sudbø, “Topological superconductivity mediated by skyrmionic magnons,” *Phys. Rev. Lett.* **130**, 156002 (2023).
- [11] Koki Mizuno and Ai Yamakage, “Magnon-mediated superconductivity at the interface between a ferromagnetic insulator and a topological crystalline insulator with wallpaper fermions,” *Phys. Rev. B* **112**, 035303 (2025).
- [12] Jacob Linder and Jason W. A. Robinson, “Superconducting spintronics,” *Nature physics* **11**, 307–315 (2015).
- [13] Tao Yu, Xi-Han Zhou, Gerrit E.W. Bauer, and I.V. Bobkova, “Electromagnetic proximity effects at heterointerfaces,” *Physics Reports* **1151**, 1–94 (2026).
- [14] Dmitry K. Efimkin and Mehdi Kargarian, “Topological spin-plasma waves,” *Physical Review B* **104**, 075413 (2021).
- [15] Anna Dyrdal, Alireza Qaiumzadeh, Arne Brataas, and Józef Barnaś, “Magnon-plasmon hybridization mediated by spin-orbit interaction in magnetic materials,” *Physical Review B* **108**, 045414 (2023).
- [16] Y. V. Bludov, J. N. Gomes, G. A. Farias, J. Fernández-

Rossier, M. I. Vasilevskiy, and N. M. R. Peres, "Hybrid plasmon-magnon polaritons in graphene-antiferromagnet heterostructures," *2D Materials* **6**, 045003 (2019).

[17] Sayandip Ghosh, Guido Menichetti, Mikhail I. Katsnelson, and Marco Polini, "Plasmon-magnon interactions in two-dimensional honeycomb magnets," *Physical Review B* **107**, 195302 (2023).

[18] Wojciech Rudziński, Mirali Jafari, Józef Barnaś, and Anna Dyrdal, "Magnon-plasmon coupling mediated by linear magnetoelectric effect in two-dimensional crystals with dzyaloshinskii-moriya interaction," *Phys. Rev. B*, – (2025).

[19] D. Quang To, Zhengtianye Wang, Yongchen Liu, Weipeng Wu, M. Benjamin Jungfleisch, John Q. Xiao, Joshua M. O. Zide, Stephanie Law, and Matthew F. Doty, "Surface plasmon-phonon-magnon polariton in a topological insulator-antiferromagnetic bilayer structure," *Phys. Rev. Mater.* **6**, 085201 (2022).

[20] H. Y. Yuan and Yaroslav M. Blanter, "Breaking surface-plasmon excitation constraint via surface spin waves," *Phys. Rev. Lett.* **133**, 156703 (2024).

[21] H. Y. Yuan, Yaroslav M. Blanter, and H. Q. Lin, "Strong and tunable coupling between antiferromagnetic magnons and surface plasmons," *Phys. Rev. B* **111**, 024422 (2025).

[22] Vemund Falch, Jeroen Danon, Alireza Qaiumzadeh, and Arne Brataas, "Impact of spin torques and spin-pumping phenomena on magnon-plasmon polaritons in antiferromagnetic insulator-semiconductor heterostructures," *Phys. Rev. B* **109**, 214436 (2024).

[23] Torsten Karzig, Charles-Edouard Bardyn, Netanel H. Lindner, and Gil Refael, "Topological polaritons," *Phys. Rev. X* **5**, 031001 (2015).

[24] Gyungchoon Go, Se Kwon Kim, and Kyung-Jin Lee, "Topological Magnon-Phonon Hybrid Excitations in Two-Dimensional Ferromagnets with Tunable Chern Numbers," *Physical Review Letters* **123**, 237207 (2019).

[25] Xiaou Zhang, Yinhai Zhang, Satoshi Okamoto, and Di Xiao, "Thermal hall effect induced by magnon-phonon interactions," *Phys. Rev. Lett.* **123**, 167202 (2019).

[26] Jiaming Luo, Shuyi Li, Zhipeng Ye, Rui Xu, Han Yan, Junjie Zhang, Gaihua Ye, Lebing Chen, Ding Hu, Xiaokun Teng, William A. Smith, Boris I. Yakobson, Pengcheng Dai, Andriy H. Nevidomskyy, Rui He, and Hanyu Zhu, "Evidence for topological magnon-phonon hybridization in a 2d antiferromagnet down to the monolayer limit," *Nano Letters* **23**, 2023–2030 (2023).

[27] Dmitry K. Efimkin and Sergey Syzranov, "Weyl excitations via helicon-phonon mixing in conducting materials," *Phys. Rev. B* **108**, L161411 (2023).

[28] B. X. Wang and C. Y. Zhao, "Topological phonon polariton enhanced radiative heat transfer in bichromatic nanoparticle arrays mimicking aubry-andré-harper model," *Phys. Rev. B* **107**, 125409 (2023).

[29] Z. Fei, A. S. Rodin, G. O. Andreev, W. Bao, A. S. McLeod, M. Wagner, L. M. Zhang, Z. Zhao, M. Thiemens, G. Dominguez, M. M. Fogler, A. H. Castro Neto, C. N. Lau, F. Keilmann, and D. N. Basov, "Gate-tuning of graphene plasmons revealed by infrared nano-imaging," *Nature (London)* **487**, 82–85 (2012).

[30] Jianing Chen, Michela Badioli, Pablo Alonso-González, Sukosin Thongrattanasiri, Florian Huth, Johann Osmund, Marko Spasenović, Alba Centeno, Amaia Pescuera, Philippe Godignon, Amaia Zurutuza Elorza, Nicolas Camara, F. Javier García de Abajo, Rainer Hillenbrand, and Frank H. L. Koppens, "Optical nano-imaging of gate-tunable graphene plasmons," *Nature* **487**, 77–81 (2012).

[31] A. N. Grigorenko, M. Polini, and K. S. Novoselov, "Graphene plasmonics," *Nature photonics* **6**, 749–758 (2012).

[32] Chenhang Xu and Alfred Zong, "Time-domain study of coupled collective excitations in quantum materials," *npj Quantum Materials* **10**, 1–19 (2025).

[33] Jing Zhang, Shuai Jia, Iskandar Kholmanov, Liang Dong, Dequan Er, Weibing Chen, Hua Guo, Zehua Jin, Vivek B. Shenoy, Li Shi, and Jun Lou, "Janus Monolayer Transition-Metal Dichalcogenides," *ACS Nano* **11**, 8192–8198 (2017).

[34] Qun-Fang Yao, Jia Cai, Wen-Yi Tong, Shi-Jing Gong, Ji-Qing Wang, Xian-gang Wan, Chun-Gang Duan, and J. H. Chu, "Manipulation of the large Rashba spin splitting in polar two-dimensional transition metal dichalcogenides," *Physical Review B* **95** (2017), 10.1103/PhysRevB.95.165401.

[35] Amirhossein Rezavand and Nayereh Ghobadi, "Tuning the rashba spin splitting in janus mosete and wsete van der waals heterostructures by vertical strain," *Journal of Magnetism and Magnetic Materials* **544**, 168721 (2022).

[36] Andrew J. Princep, Russell A. Ewings, Simon Ward, Sandor Tóth, Carsten Dubs, Dharmalingam Prabhakaran, and Andrew T. Boothroyd, "The full magnon spectrum of yttrium iron garnet," *npj Quantum Materials* **2**, 1–5 (2017).

[37] J. Mendil, M. Trassin, Q. Bu, J. Schaab, M. Baumgartner, C. Murer, P. T. Dao, J. Vijayakumar, D. Bracher, C. Bouillet, C. A. F. Vaz, M. Fiebig, and P. Gambardella, "Magnetic properties and domain structure of ultrathin yttrium iron garnet/pt bilayers," *Phys. Rev. Mater.* **3**, 034403 (2019).

[38] Sreeveni Das, Rhodri Mansell, Lukáš Flajšman, Lide Yao, and Sebastiaan van Dijken, "Perpendicular magnetic anisotropy in bi-substituted yttrium iron garnet films," *Journal of Applied Physics* **134**, 243902 (2023).

[39] L. A. Fenner, A. A. Dee, and A. S. Wills, "Non-collinearity and spin frustration in the itinerant kagome ferromagnet  $Fe_3Sn_2$ ," *Journal of Physics: Condensed Matter* **21**, 452202 (2009).

[40] X. F. Wang, "Plasmon spectrum of two-dimensional electron systems with Rashba spin-orbit interaction," *Physical Review B* **72**, 085317 (2005).

[41] S. Raghu, Suk Bum Chung, Xiao-Liang Qi, and Shou-Cheng Zhang, "Collective modes of a helical liquid," *Phys. Rev. Lett.* **104**, 116401 (2010).

[42] Dmitry K Efimkin, Yurii E Lozovik, and Alexey A Sokolik, "Collective excitations on a surface of topological insulator," *Nanoscale research letters* **7**, 163–163 (2012).

[43] D. K. Efimkin, Yu. E. Lozovik, and A. A. Sokolik, "Spin-plasmons in topological insulator," *Journal of Magnetism and Magnetic Materials* **324**, 3610–3612 (2012).

[44] (See Appendix. C) for their explicit expressions for a square lattice formed by alternating spins  $S_1$  and  $S_2$ , a minimal model for ferrimagnet.

[45] Saurabh Maiti, Vladimir Zyuzin, and Dmitrii L. Maslov, "Collective modes in two- and three-dimensional electron systems with rashba spin-orbit coupling," *Phys. Rev. B* **91**, 035106 (2015).

[46] Alexander L. Fetter, "Electrodynamics of a layered elec-

tron gas. i. single layer," *Annals of Physics* **81**, 367–393 (1973).

[47] Alexander L Fetter, "Electrodynamics of a layered electron gas. ii. periodic array," *Annals of Physics* **88**, 1–25 (1974).

[48] In our previous work, we formulated the theory describing plasmon-magnon coupling in terms of coupled response functions of charge  $\rho(\mathbf{r}, t)$  and spin-densities  $\mathbf{s}(\mathbf{r}, t)$  to the scalar potential  $\phi(\mathbf{r}, t)$  and magnetic fluctuations  $\boldsymbol{\ell}_\alpha(\mathbf{r}, t)$  evaluated using the Kubo linear-response framework. Although this formulation provides a transparent physical interpretation and enables a straightforward determination of the mixed-mode dispersion, it is not optimal for analysing their topological properties.

[49] We note that both Rashba subbands have the same Fermi velocity for positive Fermi energies [40], which is the relevant regime considered in this work.

[50] Cooper Finnigan and Dmitry K. Efimkin, "Giant resonant skew scattering of plasma waves in a two-dimensional electron gas," *Phys. Rev. B* **110**, L041406 (2024).

[51] Cooper Finnigan and Dmitry K. Efimkin, "Anomalous skew scattering of plasmons in a dirac electron fluid," *Phys. Rev. B* **111**, 165404 (2025).

[52] Cooper Finnigan, Mehdi Kargarian, and Dmitry K. Efimkin, "Equatorial magnetoplasma waves," *Phys. Rev. B* **105**, 205426 (2022).

[53] Dafei Jin, Ling Lu, Zhong Wang, Chen Fang, John D. Joannopoulos, Marin Soljačić, Liang Fu, and Nicholas X. Fang, "Topological magnetoplasmon," *Nature Communications* **7**, 13486 (2016).

[54] Nicolas Perez, Armand Leclerc, Guillaume Laibe, and Pierre Delplace, "Topology of shallow-water waves on a rotating sphere," *Journal of Fluid Mechanics* **1003**, A35 (2025).

[55] Yohei Onuki, Antoine Venaille, and Pierre Delplace, "Bulk-edge correspondence recovered in incompressible geophysical flows," *Phys. Rev. Res.* **6**, 033161 (2024).

[56] Pierre Delplace, J. B. Marston, and Antoine Venaille, "Topological origin of equatorial waves," *Science* **358**, 1075–1077 (2017).

[57] Guangyao Li and Dmitry K. Efimkin, "Equatorial waves in rotating bubble-trapped superfluids," *Phys. Rev. A* **107**, 023319 (2023).

[58] Due to the classical nature of the considered problem — spin- and current-densities are real fields — the effective Hamiltonian  $\mathcal{H}_\mathbf{q}^{\text{out}}$  respects the unbreakable particle-hole symmetry. As a result, its negative frequency eigenmodes are not dynamically independent from the positive frequency ones and do not need to be considered separately. Furthermore,  $\mathcal{H}_\mathbf{q}^{\text{out}}$  has a spurious zero-frequency mode protected by the interplay between particle-hole and inversion symmetries of the effective Hamiltonian.

[59] We note that Fig. (2) depicts the hybridization of plasmons with two distinct magnon branches. Although Eq. (7) includes only a single magnon branch, extending the effective Hamiltonian to incorporate both branches is straightforward.

[60] These include direct plasmon-magnon coupling mediated by the oscillating magnetic field, quadratic-order terms describing magnetic fluctuations,  $\mathbf{n} = \ell_x \mathbf{e}_x + \sqrt{1 - \ell_x^2 - \ell_z^2} \mathbf{e}_y + \ell_z \mathbf{e}_z \approx \ell_x \mathbf{e}_x + (1 - (\ell_x^2 + \ell_z^2)/2) \mathbf{e}_y + \ell_z \mathbf{e}_z$ , as well as higher-order contributions in the high-frequency expansion of the microscopically calculated electronic response functions (see Appendix A).

[61] Z. Fei, A. S. Rodin, G. O. Andreev, W. Bao, A. S. McLeod, M. Wagner, L. M. Zhang, Z. Zhao, M. Thiemens, G. Dominguez, M. M. Fogler, A. H. Castro Neto, C. N. Lau, F. Keilmann, and D. N. Basov, "Gate-tuning of graphene plasmons revealed by infrared nano-imaging," *Nature* **487**, 82–85 (2012).

[62] Akitoshi Shiotari, Jun Nishida, Adnan Hammud, Fabian Schulz, Martin Wolf, Takashi Kumagai, and Melanie Müller, "Scattering near-field optical microscopy at 1-nm resolution using ultralow tip oscillation amplitudes," *Science Advances* **11** (2025), 10.1126/sciadv.adu1415.

[63] T. Eberlein, U. Bangert, R. R. Nair, R. Jones, M. Gass, A. L. Bleloch, K. S. Novoselov, A. Geim, and P. R. Briddon, "Plasmon spectroscopy of free-standing graphene films," *Phys. Rev. B* **77**, 233406 (2008).

[64] R. J. Koch, Th. Seyller, and J. A. Schaefer, "Strong phonon-plasmon coupled modes in the graphene/silicon carbide heterosystem," *Phys. Rev. B* **82**, 201413 (2010).

[65] G. D. Dwivedi, C.-M. Wu, Bo-Yu Chen, S. T. Lin, W.-Z. Qiu, S. J. Sun, Guangyong Xu, J. W. Lynn, J. W. Chiou, C.-H Lee, W.-H. Li, S. Yano, and H. Chou, "Magnon profile on SrRuO<sub>3</sub> films studied by inelastic neutron scattering," *Phys. Rev. B* **101**, 054403 (2020).

[66] Shinichi Itoh, Yasuo Endoh, Tetsuya Yokoo, Soshi Ibuka, Je-Geun Park, Yoshio Kaneko, Kei S. Takahashi, Yoshi-nori Tokura, and Naoto Nagaosa, "Weyl fermions and spin dynamics of metallic ferromagnet sruo3," *Nature communications* **7**, 11788–8 (2016).

[67] Xiao-Tian Zhang, Yong Hao Gao, and Gang Chen, "Thermal hall effects in quantum magnets," *Physics Reports* **1070**, 1–59 (2024).

[68] Mahroo Shiranzaei, Roberto E Troncoso, Jonas Fransson, Arne Brataas, and Alireza Qaiumzadeh, "Thermal squeezing and nonlinear spectral shift of magnons in antiferromagnetic insulators," *New Journal of Physics* **24**, 103009 (2022).

[69] E. H. Hwang and S. Das Sarma, "Dielectric function, screening, and plasmons in two-dimensional graphene," *Phys. Rev. B* **75**, 205418 (2007).

[70] B Wunsch, T Stauber, F Sols, and F Guinea, "Dynamical polarization of graphene at finite doping," *New Journal of Physics* **8**, 318 (2006).

[71] Tobias Stauber, "Plasmonics in Dirac systems: From graphene to topological insulators," *Journal of Physics: Condensed Matter* **26**, 123201 (2014).

[72] Alexander Altland and Ben D. Simons, *Condensed Matter Field Theory*, 2nd ed. (Cambridge University Press, 2010).

[73] T. Holstein and H. Primakoff, "Field dependence of the intrinsic domain magnetization of a ferromagnet," *Phys. Rev.* **58**, 1098–1113 (1940).